Article | Open Access

Energy Materials

Chua *et al. Energy Mater.* **2026**, *6*, 600125 **DOI:**10.20517/energymater.2026.229

Exsolved nickel sites for methane decomposition to hydrogen and carbon

Song Rong Chua[1,#], Ruinan Wang[2,#], Zhihua Deng[1,3], Guoping Xiao[4], Jian-Qiang Wang[4], Hongquan He[5], Xun Cao[5], Chee Kok Poh[5], Lili Zhang[1,5], Lan Zhang[3,4,*], Meng Ni[2,*], Siew Hwa Chan[1,3,*]

Keywords:
Catalytic methane decomposition, Ni-LCCM perovskite catalyst, non-monotonic carbon productivity, density functional theory, carbon purification

Citation: Chua, S. R.; Wang, R.; Deng, Z.; Xiao, G.; Wang, J. Q.; He, H.; Cao, X.; Poh, C. K.; Zhang, L.; Zhang, L.; Ni, M.; Chan, S. H. Exsolved nickel sites for methane decomposition to hydrogen and carbon. *Energy Mater.* **2026**, *6*, 600125. https://dx.doi.org/10.20517/energymater.2026.229

Received: 18 Jul 2026
First Decision: 3 Aug 2026
Revised: 23 Aug 2026
Accepted: 26 Aug 2026
Published: 23 Sep 2026

Academic Editor:
Yuping Wu
Copy Editor:
Ping Zhang
Production Editor:
Ping Zhang

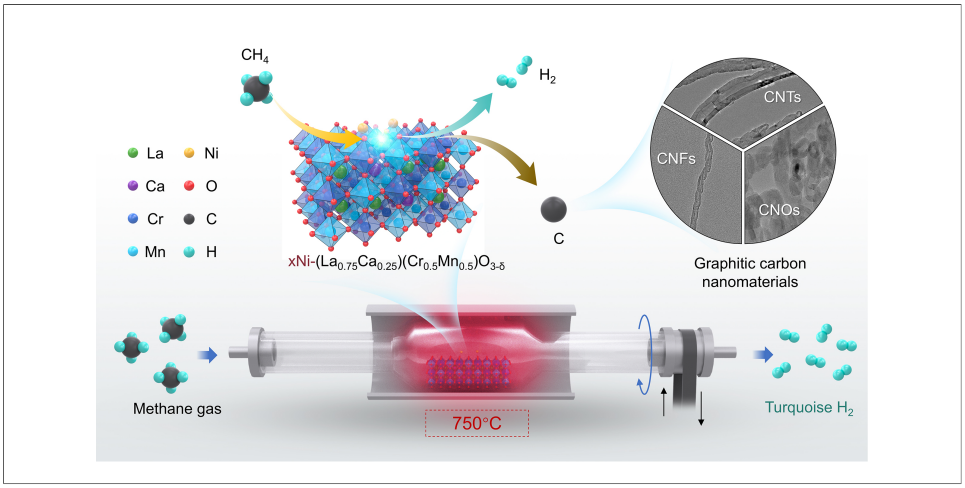

Abstract

Hydrogen production via catalytic decomposition of methane (CDM) offers a CO_2-free route for simultaneous hydrogen and solid carbon generation. However, practical implementation remains limited by catalyst deactivation, metal contamination in the carbon product, and inefficient post-reaction purification. In this work, Ni-promoted $(La_{0.75}Ca_{0.25})(Cr_{0.5}Mn_{0.5})O_{3-\delta}$ (Ni-LCCM) perovskite catalysts prepared via a nitrate-based route were evaluated for CDM. Under thermal CDM at 750 °C without pre-reduction, 050Ni-LCCM achieved a Ni-normalized carbon productivity of up to 11.53 $g_C \cdot g_{Ni}^{-1}$. A non-monotonic dependence of intrinsic carbon productivity on Ni loading was observed, with local maxima for 050Ni-LCCM and 150Ni-LCCM. These two experimental compositions were represented by the 2Ni-LCCM and 6Ni-LCCM models in the density functional theory (DFT) calculations. The 2Ni-LCCM and 6Ni-LCCM models showed lower relative rate-limiting activation barriers than those of neighboring configurations. Together with

[1]School of Mechanical and Aerospace Engineering, Nanyang Technological University, Singapore 639798, Singapore.
[2]Department of Building Environment and Energy Engineering, Research Institute for Sustainable Urban Development (RISUD) and Research Institute for Smart Energy (RISE), The Hong Kong Polytechnic University, Hong Kong 999077, China.
[3]Energy Research Institute at NTU (ERI@N), Nanyang Technological University, Singapore 637141, Singapore.
[4]State Key Laboratory of Thorium Energy, Shanghai Institute of Applied Physics, Chinese Academy of Sciences, Shanghai 201800, China.
[5]Institute of Sustainability for Chemicals, Energy and Environment (ISCE2), Agency for Science, Technology and Research (A*STAR), Singapore 627833, Singapore.
[#]These authors contributed equally to this work.

***Correspondence to:** Prof. Lan Zhang, Energy Research Institute at NTU (ERI@N), Nanyang Technological University, Singapore 637141, Singapore; State Key Laboratory of Thorium Energy, Shanghai Institute of Applied Physics, Chinese Academy of Sciences, Shanghai 201800, China. E-mail: zhanglan5678@sinap.ac.cn; Prof. Meng Ni, Department of Building Environment and Energy Engineering, Research Institute for Sustainable Urban Development (RISUD) and Research Institute for Smart Energy (RISE), The Hong Kong Polytechnic

University, Hong Kong 999077, China. E-mail: meng.ni@polyu.edu.hk; Prof. Siew Hwa Chan, School of Mechanical and Aerospace Engineering, Nanyang Technological University, Singapore 639798, Singapore; Energy Research Institute at NTU (ERI@N), Nanyang Technological University, Singapore 637141, Singapore. E-mail: mshchan@ntu.edu.sg

structural characterization, these results suggest that methane decomposition activity is strongly influenced by local Ni configuration, Ni reducibility, and site accessibility rather than by total Ni loading alone. Carbon characterization showed the formation of predominantly nanocrystalline graphitic carbon, including mixed carbon nanostructures such as carbon nanotubes, carbon nanofibers, and carbon nano-onions. Post-reaction purification using 5 M HNO_3 reduced the residual inorganic content to 4.20% and 1.41% for carbon products from 050Ni-LCCM and 150Ni-LCCM, respectively, corresponding to thermogravimetric analysis (TGA)-based carbon contents of approximately 95.8% and 98.6%. Overall, the results demonstrate that Ni-LCCM is an effective catalyst system for CDM, in which composition-dependent Ni configurations influence intrinsic carbon productivity while enabling recovery of high-carbon-content solid products after mild acid treatment.

INTRODUCTION

Hydrogen is an essential feedstock for chemical manufacturing, refining, and fuel-cell technologies, and is increasingly regarded as a key energy carrier for deep decarbonization[1,2]. Depending on the production route and associated carbon footprint, hydrogen is commonly classified as grey, blue, green, or turquoise hydrogen[3]. Grey hydrogen, mainly produced by steam methane reforming (SMR), is accompanied by substantial CO_2 emissions, whereas blue hydrogen relies on carbon capture and storage (CCS) to reduce emissions. However, CCS increases process complexity, energy consumption, and cost[4,5]. Green hydrogen from renewable-powered water electrolysis offers a low-carbon route, but its large-scale deployment is still constrained by electricity cost, electrolyzer durability, and renewable power availability. In this context, CDM has emerged as an attractive complementary route for turquoise hydrogen production, because methane can be directly converted into hydrogen and solid carbon without direct CO_2 formation[6]. The solid carbon co-product also provides an opportunity to improve process economics if it can be recovered with sufficient purity and structural quality.

Catalytic performance and the practical feasibility of CDM are strongly affected by catalyst composition, active-site structure, and carbon management. Ni-based catalysts are among the widely studied systems because of their high activity and relatively low cost[7]. In this work, Ni was selected as the modifying element because Ni is effective for C-H bond activation and can promote the formation of graphitic carbon during methane decomposition. Moreover, Ni species can interact with perovskite oxide frameworks and generate surface-enriched or exsolution-related active sites under reducing conditions and during methane decomposition.

Other transition metals, such as Fe and Co, may also affect methane decomposition, but they are not expected to behave identically to Ni because their reducibility, metal-support interaction, carbon solubility, and carbon-growth behavior can differ substantially. Therefore, this study focuses on Ni-modified LCCM as a representative system to establish the relationship between Ni loading, active-site evolution, and carbon productivity. Future work will include a systematic comparison with Fe- and Co-modified LCCM catalysts.

Nevertheless, conventional supported Ni catalysts often suffer from sintering, carbon-induced deactivation[8,9], and the incorporation of metal or support residues into the carbon product[10,11]. These issues not only shorten catalyst lifetime but also complicate the purification and downstream utilization of the produced carbon. Strategies such as bimetallic catalyst design[7,11], support modification[12,13], and reactor engineering using fluidized-bed[14] or molten-media systems[15] have been investigated to improve activity and

carbon removal. However, achieving stable hydrogen production while recovering low-residue carbon products remains challenging, especially when oxide supports or residual metal species are difficult to remove after reaction[10,16].

Perovskite-derived catalysts provide a useful platform for addressing these challenges because reducible metal species can be incorporated into the oxide lattice and subsequently exsolved as anchored nanoparticles under reducing or reaction conditions[17,18]. Compared with conventionally impregnated metal particles, exsolved nanoparticles are often partially embedded in the oxide surface, forming socketed metal-support interfaces that improve thermal stability and sintering resistance[17]. Ni-substituted La-Sr-Cr-Mn-based perovskites, $(La_{0.75}Sr_{0.25})(Cr_{0.5}Mn_{0.5-x}Ni_x)O_{3-\delta}$ and $(La_{0.75}Sr_{0.25})(Cr_{0.5-x}Ni_xMn_{0.5})O_{3-\delta}$, have been extensively studied as redox-stable electrode materials for solid oxide fuel cells (SOFCs), including symmetrical SOFC configurations[19], owing to their structural robustness under both oxidizing and reducing conditions[20,21]. Compared with Sr-based $(La_{0.75}Sr_{0.25})(Cr_{0.5}Mn_{0.5-x}Ni_x)O_{3-\delta}$ (LSCM), Ca-substituted $(La_{0.75}Ca_{0.25})(Cr_{0.5}Mn_{0.5})O_{3-\delta}$ (LCCM) can reduce lattice strain and mitigate Sr-related A-site segregation concerns[22,23]. Building on this concept, LCCM offer a stable oxide framework, while Ni incorporation provides a route to generate catalytically active metallic sites during methane decomposition[24].

Although Ni-promoted LCCM catalysts have shown promise for turquoise hydrogen and carbon nanomaterial co-production, the role of composition-tuned exsolved Ni sites in determining intrinsic activity remains insufficiently understood. In many CDM studies, catalyst performance is primarily evaluated by methane conversion, hydrogen formation rate, or total carbon yield. These metrics are important but do not fully distinguish whether additional Ni contributes to more efficient active sites or merely increases the total metal amount. Ni-normalized carbon productivity therefore provides a more direct measure of intrinsic Ni utilization. In this work, the intrinsic carbon productivity on Ni-LCCM was found to depend non-monotonically on Ni loading, indicating that catalytic performance is governed not simply by the total Ni content but by the local configuration and accessibility of exsolved Ni sites.

Herein, a series of Ni-promoted LCCM perovskite catalysts was prepared through a nitrate-based gel-casting route and evaluated for CDM under rotary-bed operation without external pre-reduction. The relationship between Ni loading, exsolved Ni configuration, intrinsic carbon productivity, and carbon product purity was systematically examined. Density functional theory (DFT) calculations were further used to rationalize how different Ni configurations influence the rate-limiting barriers for methane dehydrogenation. In addition, post-reaction mild acid treatment was applied to assess the removability of catalyst-derived residues and the potential for producing high-carbon-content solid products. This study links composition-tuned exsolved Ni sites with intrinsic methane decomposition activity and carbon purification, providing a materials-design strategy for the co-production of turquoise hydrogen and high-carbon-content solid products.

EXPERIMENTAL

Chemicals

The following chemicals were used as received from Sigma Aldrich: calcium nitrate tetrahydrate [$Ca(NO_3)_2{\cdot}4H_2O$, 99%], chromium nitrate nonahydrate [$Cr(NO_3)_3{\cdot}9H_2O$, 99%], manganese nitrate tetrahydrate [$Mn(NO_3)_2{\cdot}4H_2O$, ≥ 97.0%], and nickel nitrate hexahydrate [$Ni(NO_3)_2{\cdot}6H_2O$, 99.9%]. Acrylamide (AM, $C_2H_3CONH_2$, 99.9%), N,N'-methylenebisacrylamide (MBAM, $C_2H_3CONHCH_2NHCOC_2H_3$, 99.9%), ammonium persulfate [APS, $(NH_4)_2S_2O_8$, 99.9%], and N,N,N',N'-Tetramethyl ethylenediamine (TEMED, 99.9%) were also used for gel-casting. Lanthanum nitrate hexahydrate [$La(NO_3)_3{\cdot}6H_2O$, 99.9%] was used as received from Alfa Aesar. Milli-Q deionized water (18.2 MΩ·cm) was used during all experimental procedures.

Table 1. Nominal compositions of xNi-LCCM catalysts and the corresponding representative yNi-LCCM DFT models

Sample (xNi-LCCM)	Representative DFT model (yNi-LCCM)	Ni	La	Ca	Cr	Mn
LCCM	LCCM	0.00	0.75	0.25	0.50	0.50
025Ni-LCCM	1Ni-LCCM	0.25	0.75	0.25	0.50	0.50
050Ni-LCCM	2Ni-LCCM	0.50	0.75	0.25	0.50	0.50
075Ni-LCCM	3Ni-LCCM	0.75	0.75	0.25	0.50	0.50
100Ni-LCCM	4Ni-LCCM	1.00	0.75	0.25	0.50	0.50
125Ni-LCCM	5Ni-LCCM	1.25	0.75	0.25	0.50	0.50
150Ni-LCCM	6Ni-LCCM	1.50	0.75	0.25	0.50	0.50
175Ni-LCCM	7Ni-LCCM	1.75	0.75	0.25	0.50	0.50
200Ni-LCCM	8Ni-LCCM	2.00	0.75	0.25	0.50	0.50

In the experimental notation xNi-LCCM, x denotes the sample-specific Ni-loading designation (x = 025-200). In the DFT notation yNi-LCCM, y denotes the number of Ni atoms introduced into the selected computational cell rather than the exact experimental stoichiometry. The ICP-OES-measured Ni:La:Ca:Cr:Mn molar ratio for the representative 050Ni-LCCM sample was 0.44:0.75:0.21:0.44:0.46, close to the nominal ratio of 0.50:0.75:0.25:0.50:0.50. Detailed batch information is provided in Supplementary Table 1. DFT: Density functional theory; LCCM: $(La_{0.75}Ca_{0.25})(Cr_{0.5}Mn_{0.5})O_{3-\delta}$.

Synthesis of xNi-LCCM catalysts

The xNi-LCCM catalyst series was synthesized by a water-based gel-casting method adapted from a previous report[24]. Hydrated metal nitrates were used as precursor salts instead of the oxide- and carbonate-based precursors used in earlier procedures. The catalysts were denoted according to the nominal molar amount of Ni introduced into the fixed LCCM composition; for example, 050Ni-LCCM has a nominal Ni:La:Ca:Cr:Mn molar ratio of 0.50:0.75:0.25:0.50:0.50. The nominal molar compositions are listed in Table 1.

A 50 wt% aqueous solution of each hydrated nitrate salt was prepared from $La(NO_3)_3{\cdot}6H_2O$, $Ca(NO_3)_2{\cdot}4H_2O$, $Cr(NO_3)_3{\cdot}9H_2O$, $Mn(NO_3)_2{\cdot}4H_2O$, and $Ni(NO_3)_2{\cdot}6H_2O$. To prepare 050Ni-LCCM, the corresponding nitrate solutions were mixed and stirred for 30 min, followed by the addition of 16.54 g acrylamide (AM) and 1.10 g MBAM. After stirring for another 15 min, polymerization was initiated by sequentially adding 16.54 g of 2 wt% APS solution and 16.54 g of 2 wt% TEMED solution.

Figure 1 illustrates the nitrate-based aqueous gel-casting synthesis procedure for the xNi-LCCM catalysts. The nitrate-based aqueous route avoids organic solvents such as ethanol and isopropanol and offers a simple, scalable approach for preparing composition-tuned Ni-LCCM catalysts.

Materials characterization

The molar ratios of metal elements in the catalysts were determined by inductively coupled plasma optical emission spectroscopy (ICP-OES, Avio 200, PerkinElmer, USA). Calibration curves were established for Ca, Cr, La, Mn, and Ni. Calibration concentrations ranged from 1-100 ppm for Ca, Cr, La, and Ni, while Mn was calibrated over 1-20 ppm. Ni was measured using the axial viewing mode, whereas all other elements were analyzed in radial viewing mode. All calibration curves showed good linearity ($R^2 > 0.99$). Phase structures of the catalysts and carbon products were analyzed by powder X-ray diffraction (XRD, Philips MPD 1880, PANalytical, Netherlands) using Cu Kα radiation (λ = 1.5406 Å) at room temperature, and the diffraction patterns were recorded over a 2θ range of 20°-80° at a scan rate of 4° min^{-1}. Surface chemical states were examined by X-ray photoelectron spectroscopy (XPS, ESCALAB 250Xi, Thermo Fisher Scientific, USA) with an Al Kα source (hν = 1,486.6 eV), operating at an accelerating voltage of 15 kV and a filament current of 10 mA. Each spectrum was accumulated over five scans to improve the signal-to-noise ratio. The pass energy was set to 30 eV for high-resolution spectra (step size: 0.05 eV), while 100 eV was used for survey spectra.

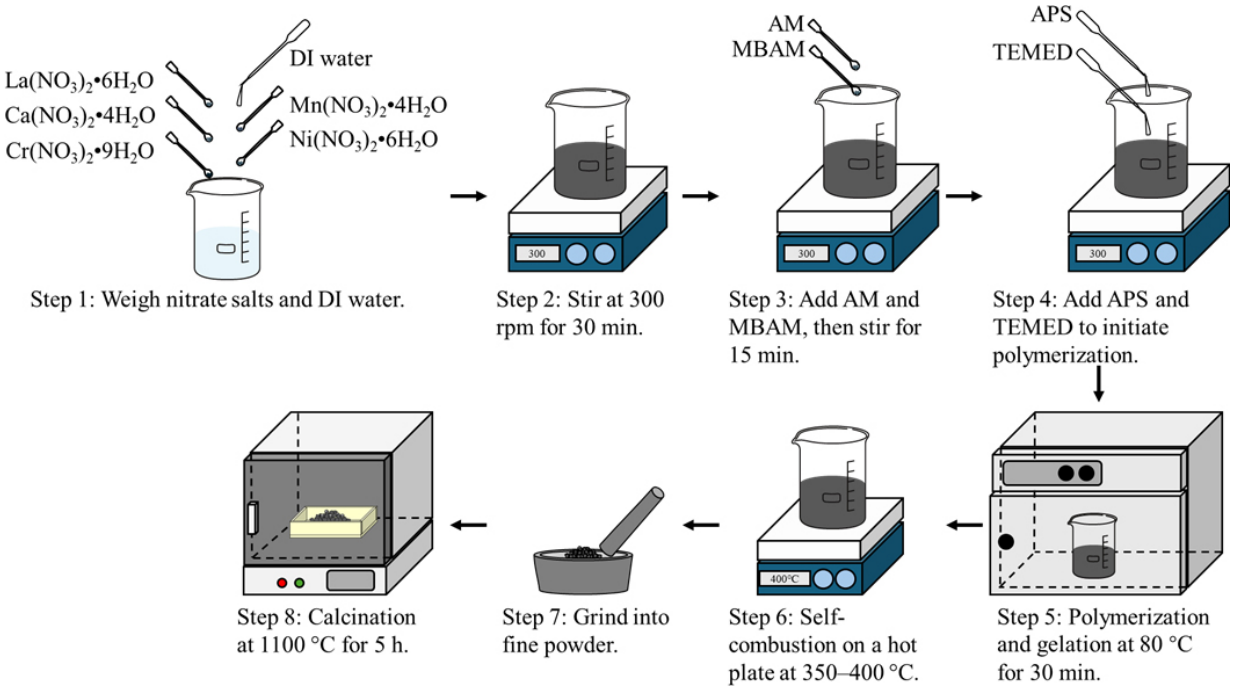

Figure 1. Schematic illustration of the nitrate-based aqueous gel-casting synthesis procedure for xNi-LCCM catalysts. AM: Acrylamide; APS: ammonium persulfate; LCCM: $(La_{0.75}Ca_{0.25})(Cr_{0.5}Mn_{0.5})O_{3-\delta}$; MBAM: N,N'-methylenebisacrylamide; TEMED: N,N,N',N'-tetramethyl ethylenediamine; DI: deionized water.

The morphology and microstructure of the catalysts and carbon products were characterized by field-emission scanning electron microscopy (FESEM, JEOL7600, JEOL, Japan), high-resolution transmission electron microscopy (HRTEM, Talos F200X, Thermo Fisher Scientific, USA), and high-angle annular dark-field scanning transmission electron microscopy (HAADF-STEM, Talos F200X, Thermo Fisher Scientific, USA) equipped with energy-dispersive X-ray spectroscopy (EDS). The FESEM observations were performed at an accelerating voltage of 5 kV, while the HRTEM and HAADF-STEM analyses were conducted at 200 kV.

H_2 temperature-programmed reduction (H_2-TPR) was carried out using an Autochem II 2920 analyzer (Micromeritics, USA). The samples were pretreated at 200 °C for 0.5 h to remove moisture, followed by heating from 50 °C to 900 °C at a ramp rate of 10 °C min^{-1} under a 10% H_2/90% Ar flow. Thermogravimetric analysis (TGA, Q500, TA Instruments, USA) was used to investigate the thermal behavior of the produced carbon nanomaterials. Approximately 10-15 mg of carbon or carbon-catalyst mixture was placed in the sample pan. The analysis was conducted at a heating rate of 10 °C min^{-1} up to 900 °C under a mixed gas flow of 40 mL min^{-1} N_2 and 60 mL min^{-1} air. Prior to analysis, the pan was pre-cleaned by heating to 900 °C at 50 °C min^{-1} to remove contaminants. Raman spectroscopy (inVia Raman microscope, Renishaw, UK) was used to evaluate carbon products. It was equipped with a 532 nm excitation laser, and the spectra were recorded over the range of 0-3,200 cm^{-1}. The obtained spectra were baseline-corrected and deconvoluted using Lorentzian functions to analyze the D, G, and 2D bands.

Catalytic activity experiments

Catalytic decomposition of methane (CDM) experiments were carried out in a rotary-bed reactor. For each test, 2 g of catalyst was loaded at the center of a specially shaped quartz tube with an inner diameter of 60 mm, an expanded central section of 100 mm, and a total length of 1.2 m [Supplementary Figure 1]. The catalyst was used directly without prior reduction under H_2. Before the reaction, the system was evacuated

with a vacuum pump to remove residual air. Methane (CH_4, 99.9%) was then introduced into the reactor at a flow rate of 100 sccm, corresponding to a space velocity of 3 $L \cdot g_{cat.}^{-1} \cdot h^{-1}$. The reactor (BTF-1200C-R-PECVD-AD, Anhui BEQ Equipment Technology, China) was rotated at 1 rpm during the reaction [Supplementary Figure 2]. The reactor was heated to the target temperature at a heating rate of 5 °C·min^{-1}. After the reaction, the CH_4 flow was stopped, and N_2 was introduced to terminate the reaction and prevent further carbon formation. The gaseous products were quantified using a gas chromatograph equipped with a thermal conductivity detector (TCD, Shimadzu Nexis GC-2030, Shimadzu, Japan). Methane conversion (X_{CH_4}, %) was calculated based on either the inlet and outlet methane amounts or the outlet hydrogen amount, assuming hydrogen and carbon as the only products. Carbon productivity was determined by normalizing the mass of deposited carbon to either the total catalyst mass ($g_C \cdot g_{cat.}^{-1}$) or the Ni mass in the catalyst ($g_C \cdot g_{Ni}^{-1}$), according to the following equations:

$$X_{CH_4}(\%) = \frac{n_{CH_4,in} - n_{CH_4,out}}{n_{CH_4,in}} \times 100\% \quad (1)$$

$$X_{CH_4}(\%) = \frac{\frac{1}{2} n_{H_2,out}}{\frac{1}{2} n_{H_2,out} + n_{CH_4,out}} \times 100\% \quad (2)$$

Where $n_{CH_4,in}$, $n_{CH_4,out}$, and $n_{H_2,out}$ denote the amounts of methane at the inlet, methane at the outlet, and hydrogen at the outlet, respectively.

$$g_C \cdot g_{cat.}^{-1} = \frac{m_t - m_{cat.}}{m_{cat}} \quad (3)$$

$$g_C \cdot g_{Ni}^{-1} = \frac{m_t - m_{cat.}}{m_{Ni}} \quad (4)$$

Where m_t is the total mass of the carbon and catalyst mixture after reaction, $m_{cat.}$ is the initial catalyst mass, and m_{Ni} is the nominal mass of Ni in the catalyst.

Reproducibility of the catalytic tests was evaluated using independent experiments under identical reaction conditions. For the Ni-loading-dependent catalytic tests, each catalyst composition was evaluated using three independent experiments. Unless otherwise stated, the reported values represent the mean of the independent measurements, with error bars indicating the corresponding standard deviation.

Purification of carbon

The as-produced carbon was purified by nitric acid treatment to remove residual metal species. Briefly, 10 mL of 5 M HNO_3 solution was added per gram of carbon product. The suspension was stirred and heated in an oil bath at 120 °C for 5 h. After acid treatment, the suspension was diluted with deionized water, mixed, and allowed to settle before solid-liquid separation. The acid-treated carbon was collected by filtration and dried at 120 °C for 24 h.

Density functional theory calculations

All calculations were performed based on DFT. The exchange-correlation functional was described using the generalized gradient approximation (GGA) with the Perdew-Burke-Ernzerhof (PBE), together with the DFT-D3 dispersion correction[25]. For geometry and lattice optimization, the plane-wave cutoff energy was set to 500 eV, and Brillouin zone integration was performed using a 4 × 4 × 1 Monkhorst-Pack k-point mesh[26]. The convergence criteria for ionic relaxation and electronic self-consistent calculations were set to 0.05 eV $Å^{-1}$ and 10^{-5} eV, respectively.

A 2 × 2 × 1 LCCM supercell exposing the (0-10) surface was constructed, with a 15 Å vacuum layer applied perpendicular to the surface. Different numbers of Ni atoms were introduced into the supercell to represent different relative Ni-loading levels and local Ni configurations. As summarized in Table 1, the yNi-LCCM

models represent computational analogs of the experimental xNi-LCCM series, rather than the exact bulk stoichiometry of the catalysts. The pristine LCCM surface corresponds to y = 0. A pure Ni(111) slab with a comparable cell size was also constructed as a reference.

The adsorption energy was calculated as:

$$\Delta E = E_{tot} - E_{sub} - E_{ad} \quad (5)$$

where E_{tot} is the total energy of the adsorbate-substrate system, E_{sub} is the energy of the bare substrate, and E_{ad} is the energy of the isolated adsorbate.

The climbing-image nudged elastic band (CI-NEB) method was used to locate transition states[27,28]. Ten images were used between the initial and final states for each elementary C-H bond cleavage step. For configurations where the initial and final states differed significantly in energy, forward and reverse activation barriers were calculated as:

$$\Delta E_R = E_{TS} - E_I \quad (6)$$

$$\Delta E_P = E_{TS} - E_F \quad (7)$$

Where E_{TS}, E_I, and E_F are the total energies of the transition state, initial state, and final state, respectively. Only the forward reaction was considered in this work; therefore, the activation energy was defined as:

$$E_a = \Delta E_R \quad (8)$$

RESULTS AND DISCUSSION

Synthesis and compositional verification of xNi-LCCM

ICP-OES analysis was used to verify the elemental compositions of the nitrate-derived xNi-LCCM catalysts. For the representative 050Ni-LCCM sample, the measured Ni:La:Ca:Cr:Mn molar ratio was close to the nominal composition, confirming that the nitrate-based gel-casting route effectively incorporated the metal precursors into the multicomponent catalyst system[29]. The measured composition of 050Ni-LCCM is provided in the note to Table 1, and the ICP-OES-derived molar ratios for individual batches and the normalization basis are provided in the Supplementary Materials [Supplementary Table 1].

XRD patterns of the calcined xNi-LCCM catalysts confirm the formation of the LCCM perovskite phase across all compositions [Figure 2A]. The diffraction peaks are consistent with previously reported LCCM structures[24], indicating that the nitrate-based gel-casting route successfully produces the targeted perovskite phase. In our previous work, xNi-LCCM catalysts were prepared using oxide and carbonate raw materials through a water-based gel-casting slurry route[24]. By contrast, the present synthesis uses hydrated metal nitrates to form a homogeneous aqueous precursor solution before polymerization and self-combustion. Despite this change in precursor chemistry and gel-casting medium from slurry to solution, the final calcined catalysts exhibit the same LCCM perovskite framework, suggesting that the nitrate-derived route does not adversely affect phase formation. With increasing Ni incorporation, the perovskite reflections show a slight shift toward higher 2q values [Figure 2B], suggesting lattice modification associated with metal incorporation and defect formation[19,29-31].

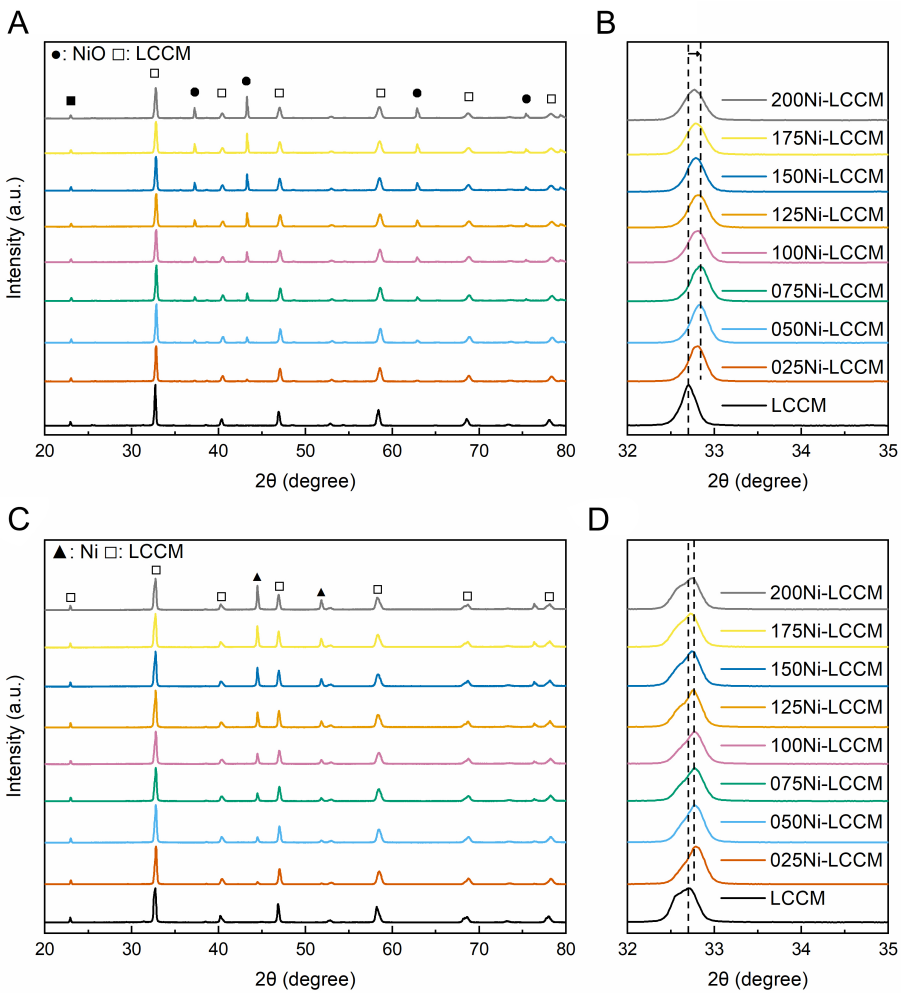

Figure 2. XRD patterns of xNi-LCCM catalysts with different Ni loadings: (A) catalysts calcined at 1,100 °C for 5 h in air; (B) enlarged view of the 2θ range of 32°-35° for the calcined catalysts; (C) catalysts reduced at 750 °C for 2 h in H_2/N_2; and (D) enlarged view of the 2θ range of 32°-35° for the reduced catalysts. Diffraction peaks corresponding to LCCM, NiO, and metallic Ni are indicated. XRD: X-ray diffraction; LCCM: $(La_{0.75}Ca_{0.25})(Cr_{0.5}Mn_{0.5})O_{3-\delta}$.

After reduction in H_2/N_2, metallic Ni reflections appear in the Ni-containing samples, while the LCCM perovskite structure remains intact [Figure 2C and D]. This confirms the reduction of Ni species[24,32,33] and the structural stability of the LCCM under reducing conditions[20]. The intensity of the metallic Ni reflections increases with Ni loading, consistent with the higher Ni content in the catalyst series.

XPS was employed to examine the surface chemical states of xNi-LCCM catalysts before and after reduction [Figure 3A-D]. Interpretation of the Ni 2p region is complicated by its overlap with La 3d signals[34,35]. Nevertheless, constrained peak deconvolution can identify characteristic Ni features[30,36,37]. After reduction, the component at ~852.3 eV is assigned to metallic Ni^0, while the features at ~855.5 eV, together with the shake-up satellite at ~861 eV, indicate the presence of Ni^{2+} species in a NiO-like environment or in the near-surface region of the perovskite lattice[38]. Contributions from La^{3+} are observed in the overlapping regions at ~850 eV and ~855-856 eV, consistent with La 3d emission[39].

To further verify the Ni chemical states, the Ni 3p region was analyzed. The spectra show signatures of metallic Ni^0 at ~66.3 eV and Ni^{2+} at ~67.6 eV, together with the corresponding shake-up satellite features [Figure 3C and D][40-42]. Owing to the spectral overlap between Ni 3p, Cr 3p, and Mn 3p signals, Cr- and

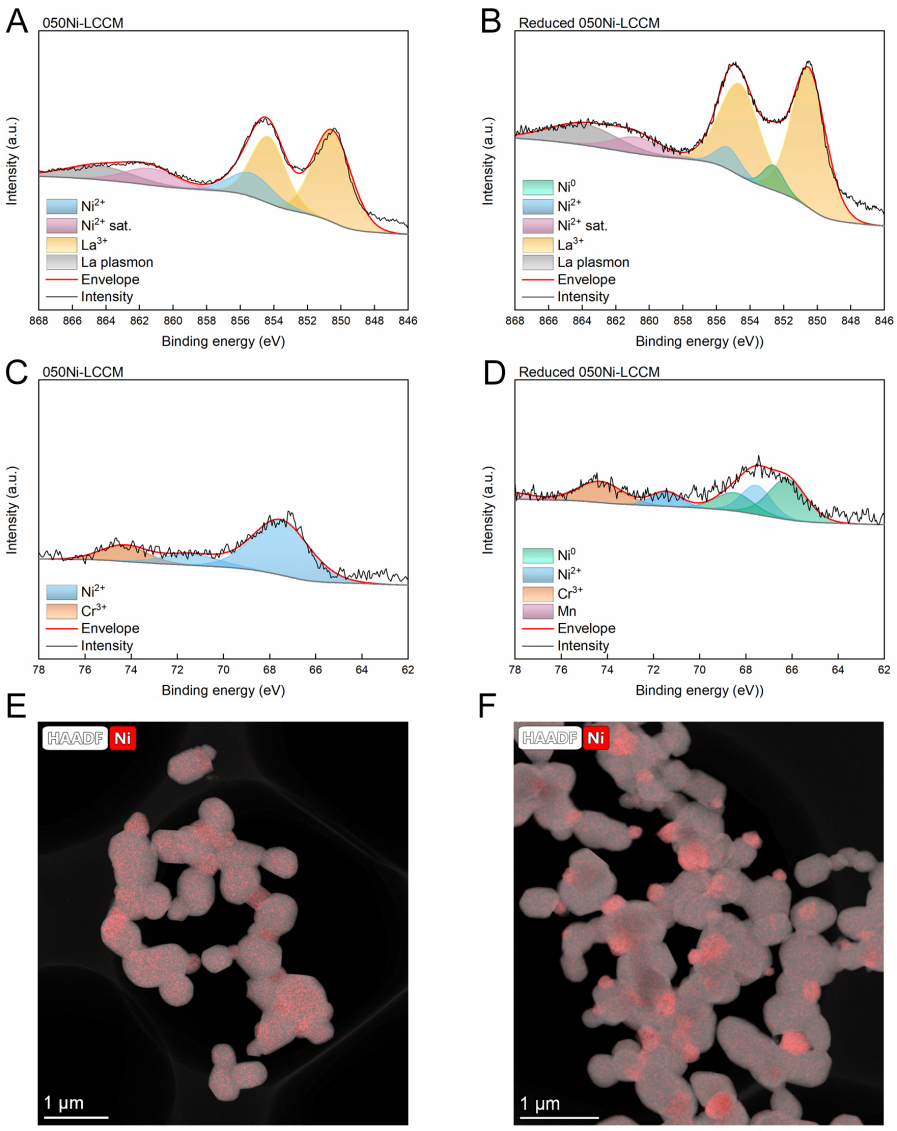

Figure 3. Surface Ni chemical states and reduction-induced Ni redistribution in 050Ni-LCCM. (A-D) XPS spectra of 050Ni-LCCM before and after reduction at 750 °C in H_2/N_2; (E and F) HAADF-STEM images and corresponding STEM-EDS Ni elemental maps of 050Ni-LCCM before and after reduction. The Ni EDS signal is displayed in red. HAADF-STEM: High-angle annular dark-field scanning transmission electron microscopy; XPS: X-ray photoelectron spectroscopy; EDS: energy-dispersive X-ray spectroscopy; LCCM: $(La_{0.75}Ca_{0.25})(Cr_{0.5}Mn_{0.5})O_{3-\delta}$.

Mn-related components were included in the deconvolution where required to obtain a reliable fit. The coexistence of Ni^0 and Ni^{2+} after reduction indicates partial reduction of Ni species, consistent with Ni exsolution from the perovskite lattice and partial surface oxidation of the exsolved nanoparticles[43,44]. Complete spectra for all compositions are provided in the Supplementary Materials [Supplementary Figures 3 and 4]

STEM-EDS mapping was further used to visualize the spatial redistribution of Ni in 050Ni-LCCM before and after reduction [Figure 3E and F]. In the calcined catalyst, the Ni signal is relatively homogeneous across the LCCM particles, indicating that Ni species are well dispersed within or on the oxide framework after the nitrate-based gel-casting and calcination process. After reduction in H_2/N_2, localized Ni-rich regions become more evident, suggesting the migration and enrichment of Ni species toward the particle surface. This observation is consistent with the XRD results, where metallic Ni reflections appear after reduction while the

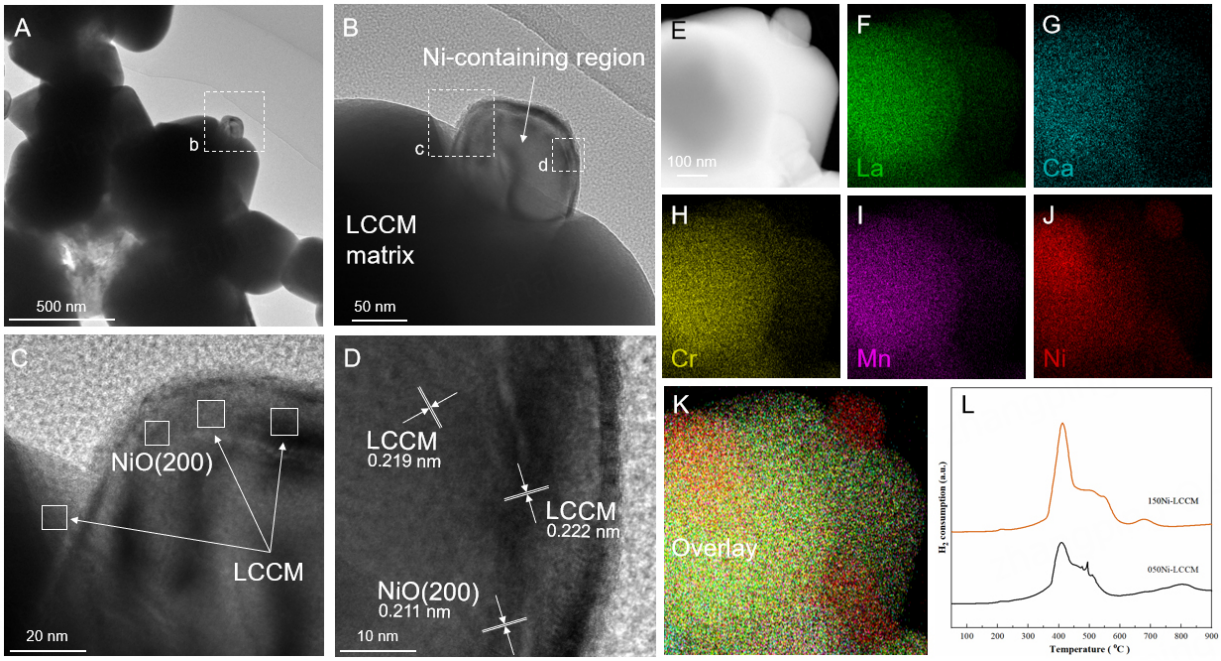

Figure 4. Ni-LCCM interfacial anchoring, elemental distribution, and reducibility of representative xNi-LCCM catalysts. (A) Low-magnification TEM image of 100Ni-LCCM showing a Ni-containing region at the LCCM matrix. (B) Enlarged TEM image of the selected interfacial region; (C and D) HRTEM images showing lattice fringes assigned to NiO and LCCM in the interfacial region; (E-K) STEM-EDS elemental mapping of the selected region: (E) HAADF image, (F) La, (G) Ca, (H) Cr, (I) Mn, (J) Ni, and (K) corresponding elemental overlay; (l) H_2-TPR profiles of 050Ni-LCCM and 150Ni-LCCM catalysts after calcination in air at 1,100 °C for 5 h. HRTEM: High-resolution transmission electron microscopy; STEM: scanning transmission electron microscopy; EDS: energy-dispersive X-ray spectroscopy; H_2-TPR: H_2 temperature-programmed reduction; LCCM: $(La_{0.75}Ca_{0.25})(Cr_{0.5}Mn_{0.5})O_{3-\delta}$; TEM: transmission electron microscopy.

LCCM perovskite framework remains intact, confirming that Ni species are reduced without collapse of the parent oxide structure. The XPS analysis further supports this interpretation by showing the coexistence of metallic Ni^0 and residual Ni^{2+} species after reduction, indicating partial reduction and possible surface oxidation of reduced Ni species.

Together, the XRD, XPS, and STEM-EDS results show that the nitrate-derived 050Ni-LCCM catalyst undergoes reduction-induced Ni redistribution while retaining the LCCM perovskite backbone. The emergence of Ni-rich surface regions provides microscopic evidence for reduction-induced Ni enrichment, consistent with the formation of surface-enriched/exsolved Ni species. These surface-enriched Ni species are expected to contribute to methane activation, while the stable LCCM framework helps maintain structural integrity under reducing conditions. This also confirms that replacing the previous oxide/carbonate-based slurry gel-casting route with a nitrate-based solution gel-casting route does not compromise the formation or redox stability of the LCCM-based catalyst.

HRTEM analysis of the 100Ni-LCCM catalyst was conducted as a representative case because of its clearly resolved interfacial features [Figure 4]. The low-magnification transmission electron microscopy (TEM) image shows aggregated catalyst particles [Figure 4A], while the enlarged TEM image reveals a Ni-containing region located at the LCCM matrix interface [Figure 4B]. Further magnification of the left and right dashed regions in Figure 4B shows the HRTEM images in Figure 4C and D, respectively. In these interfacial regions, lattice spacings of 0.211 nm are assigned to NiO(200), while spacings of 0.219-0.222 nm are attributed to the LCCM perovskite lattice. The coexistence of Ni-containing and LCCM lattice fringes within the same interfacial region indicates intimate contact between the Ni-containing phase and the oxide support.

This interfacial structure is consistent with the preceding XRD and XPS results. XRD shows that Ni-containing phases appear after reduction while the LCCM perovskite framework remains intact, and XPS reveals the coexistence of metallic Ni^0 and Ni^{2+} species after reduction. The before-and-after STEM-EDS comparison in Figure 3E and F provides direct evidence for reduction-induced Ni redistribution and local Ni enrichment in 050Ni-LCCM. In contrast, Figure 4E-K shows the local elemental distribution in the selected interfacial region of 100Ni-LCCM. Together with the HRTEM observations in Figure 4A-D, these results support the formation of Ni-containing domains anchored to the LCCM matrix. The partially embedded morphology of these domains suggests a socketed particle-support interface, which is characteristic of exsolution-derived or strongly anchored nanoparticles rather than physically detached Ni particles.

Across the catalyst series [Supplementary Figures 5-8], lattice spacings of 0.218-0.222 nm and 0.276-0.278 nm are consistently assigned to the LCCM perovskite support, while spacings of 0.208-0.213 nm correspond to NiO(200). Additional spacings of 0.244-0.245 nm are associated with Ni-containing oxide domains, and in the 150Ni-LCCM sample [Supplementary Figure 8], a spacing of ~0.179 nm is consistent with metallic Ni(200), indicating a higher degree of Ni reduction at higher Ni loadings. Overall, the coexistence of Ni-containing and LCCM lattice fringes, together with the observed interfacial anchoring, supports strong metal-support integration in the xNi-LCCM catalysts.

H_2-TPR was conducted on 050Ni-LCCM and 150Ni-LCCM to further probe the reducibility of Ni species and their interaction with the LCCM framework [Figure 4L]. Both samples exhibit a main reduction peak centered at ~400 °C, together with a broad shoulder in the range of 450-550 °C. The low-temperature reduction peak becomes more intense with increasing Ni loading, indicating a larger amount of reducible NiO-like species that are more accessible to H_2. This assignment is consistent with the XRD results, where NiO reflections are observed after calcination and metallic Ni reflections appear after reduction.

The shoulder at higher temperature is attributed to Ni species that interact more strongly with the LCCM perovskite lattice or are partially incorporated near the oxide framework. Such species require higher temperatures for reduction than surface NiO-like species[45,46]. This behavior is consistent with previous studies showing that Ni species with stronger interactions with the support or lattice incorporation exhibit higher reduction temperatures than surface Ni species[47]. Comparable multi-step reduction features have also been reported for Ni-containing perovskites, where reduction peaks in the ~400-600 °C range are associated with the progressive reduction of lattice-incorporated Ni species[48]. Together with the XPS results showing the coexistence of metallic Ni^0 and residual Ni^{2+} after reduction, the before-and-after STEM-EDS comparison in Figure 3E and F, and the interfacial TEM/STEM-EDS observations in Figure 4A-K, the H_2-TPR profiles further support the presence of multiple Ni environments in Ni-LCCM catalysts, including accessible surface NiO-like species and more strongly bound lattice-associated Ni species. These different Ni environments are expected to contribute to the formation of surface-enriched/exsolved Ni sites during reduction and subsequent methane decomposition.

To correlate the Ni-loading-dependent increase in reducible Ni species observed by H_2-TPR with catalyst morphology, FESEM was used to examine the calcined xNi-LCCM catalysts after treatment in air at 1,100 °C for 5 h. The corresponding images and particle size distributions are provided in the Supplementary Materials [Supplementary Figure 9]. These morphology data provide additional context for understanding how Ni loading affects the distribution and accessibility of reducible Ni species.

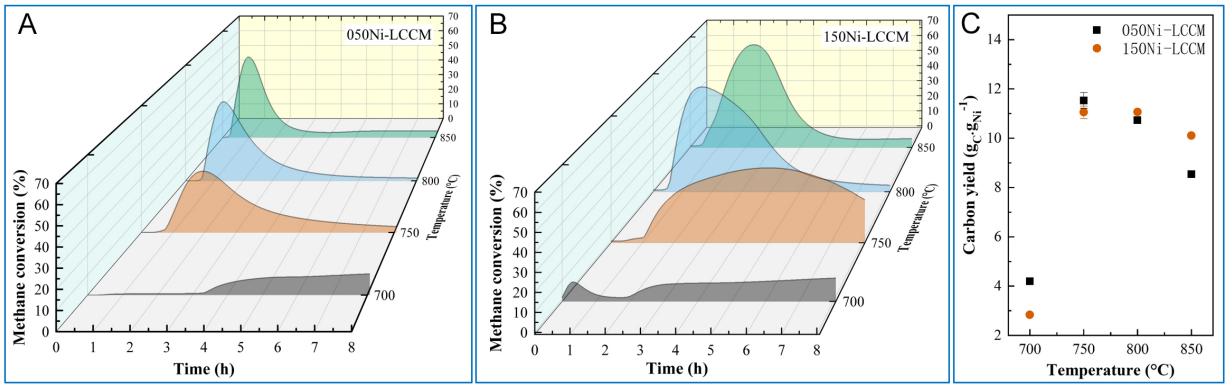

Figure 5. Effect of reaction temperature on methane conversion and Ni-normalized carbon productivity over 050Ni-LCCM and 150Ni-LCCM catalysts. (A and B) Methane conversion as a function of time on stream over (A) 050Ni-LCCM and (B) 150Ni-LCCM at 700-850 °C; (C) Ni-normalized carbon productivity at different reaction temperatures. The experiments were conducted in a rotary reactor at 1 rpm for 8 h with a space velocity of 3 $L \cdot g_{cat.}^{-1} \cdot h^{-1}$. Error bars represent the standard deviation of three independent tests performed at 750 °C. This temperature was selected as the representative reaction condition for reproducibility verification. LCCM: $(La_{0.75}Ca_{0.25})(Cr_{0.5}Mn_{0.5})O_{3-\delta}$.

Evaluation of catalytic activity in CDM

Effect of reaction temperature

The effect of reaction temperature was evaluated using 050Ni-LCCM and 150Ni-LCCM, which were selected as representative compositions for comparing Ni utilization and catalytic stability. As discussed above, XRD, XPS, STEM-EDS, and H_2-TPR results indicate that increasing Ni loading increases the amount of reducible Ni species and promotes the formation of surface-enriched Ni-containing domains, while the LCCM framework remains structurally stable under reducing conditions. These structural features are expected to influence methane activation and catalyst deactivation during CDM.

Increasing the reaction temperature from 700 to 750 °C markedly enhanced methane conversion and Ni-normalized carbon productivity [Figure 5][3]. At 700 °C, methane activation was limited, resulting in low conversion and low carbon productivity. Raising the temperature to 750 °C improved methane decomposition kinetics and gave the highest Ni-normalized carbon productivity for 050Ni-LCCM, while 150Ni-LCCM showed a slightly higher value at 800 °C. Further increasing the temperature to 800-850 °C generally increased the initial methane conversion but also accelerated deactivation. At 850 °C, the Ni-normalized carbon productivity decreased for both catalysts.

This temperature-dependent behavior suggests a trade-off between methane activation and catalyst stability. Higher temperatures facilitate C-H bond activation and initially increase methane conversion, but they may also accelerate Ni migration, sintering, or carbon encapsulation, thereby reducing the number of accessible active sites during prolonged operation. This interpretation is consistent with the H_2-TPR and microscopy results, which show that Ni species exist in multiple environments and that reducible Ni-rich regions form under reducing conditions. Considering the overall balance among activity, Ni-normalized carbon productivity, and catalytic stability under rotary-bed operation, 750 °C was selected as the representative reaction temperature for subsequent studies.

Non-monotonic Ni utilization in xNi-LCCM catalysts

The catalytic performance of the xNi-LCCM series was evaluated at 750 °C under rotary-bed operation to examine the effect of Ni loading on methane decomposition. Here, x denotes the sample-specific Ni-loading designation (x = 025-200), with the corresponding nominal Ni:La:Ca:Cr:Mn molar compositions provided in Table 1. Methane conversion generally increases with increasing Ni loading, indicating that a higher Ni

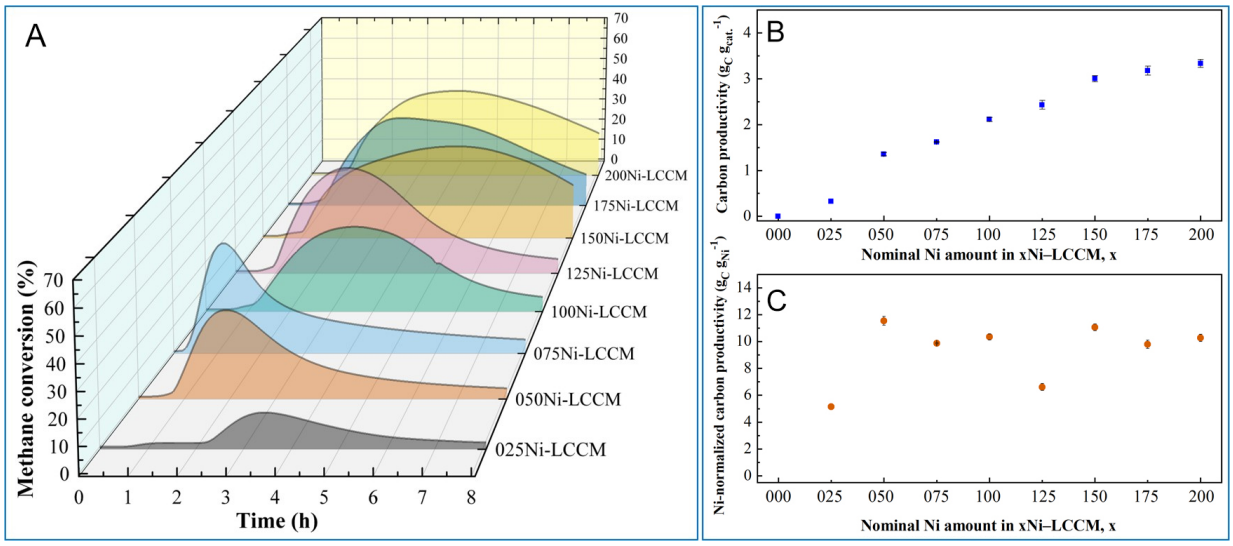

Figure 6. Ni-loading-dependent methane decomposition performance and carbon productivity of xNi-LCCM catalysts at 750 °C. (A) Methane conversion as a function of time on stream over xNi-LCCM catalysts; (B) Catalyst-mass-normalized carbon productivity; (C) Ni-normalized carbon productivity. The experiments were conducted in a rotary reactor at 750 °C and 1 rpm for 8 h with a space velocity of 3 $L \cdot g_{cat.}^{-1} \cdot h^{-1}$. Error bars represent the standard deviation of repeated measurements (n = 3 independent tests). LCCM: $(La_{0.75}Ca_{0.25})(Cr_{0.5}Mn_{0.5})O_{3-\delta}$.

content provides more reducible Ni species and improves the overall methane activation capacity [Figure 6A]. This trend is consistent with the H_2-TPR results, which show a larger amount of reducible NiO-like species at higher Ni loading, and with the XRD/XPS results showing the formation of metallic Ni-containing species after reduction. Lower-Ni samples deactivate more rapidly, whereas higher-Ni samples maintain more stable conversion over 8 h at 750 °C.

The carbon yield determined from post-reaction mass collection was independently verified by thermogravimetric analysis, confirming the reliability of the gravimetric measurements [Supplementary Table 2]. For the Ni-free LCCM (x = 000), no measurable carbon formation was detected in repeated experiments, consistent with the FESEM observations showing essentially unchanged LCCM particle surfaces after reaction. Accordingly, Ni-normalized carbon productivity is not applicable to this sample and is omitted from Figure 6C. When normalized by catalyst mass, the carbon productivity ($g_C \cdot g_{cat.}^{-1}$) increases monotonically with Ni loading [Figure 6B], following the trend in methane conversion. This indicates that increasing total Ni content enhances the overall carbon formation capacity of the catalyst. However, when the carbon yield is normalized by Ni content ($g_C \cdot g_{Ni}^{-1}$), the productivity does not scale proportionally with the amount of Ni [Figure 6C]. Instead, Ni-normalized carbon productivity shows a non-monotonic dependence on Ni loading, with local maxima at x = 050 and x = 150, while neighboring compositions display lower values.

This non-monotonic behavior suggests that Ni utilization is not determined solely by the total Ni content, but is also strongly influenced by the local configuration, reducibility, and accessibility of Ni species in the LCCM framework. The structural characterization above supports this interpretation: XRD confirms that the LCCM framework remains stable after reduction, XPS shows the coexistence of Ni^0 and Ni^{2+} species, the before-and-after STEM-EDS comparison in Figure 3E and F reveals reduction-induced Ni redistribution, and HRTEM/STEM-EDS analysis in Figure 4A-K indicates local Ni enrichment and interfacial anchoring between Ni-containing domains and the LCCM matrix. Therefore, increasing Ni loading can improve total methane conversion, but excessive or less accessible Ni may contribute less efficiently to intrinsic carbon productivity.

Table 2. Correlation between experimental Ni-normalized carbon productivity and representative DFT models for xNi-LCCM catalysts

Experimental sample	Nominal Ni/LCCM molar ratio	DFT model	Ni-normalized carbon productivity, $g_C g_{Ni}^{-1}$	Rate-limiting activation barrier, eV
LCCM	0.00	LCCM	N/A	5.88
025Ni-LCCM	0.25	1Ni-LCCM	5.70	4.86
050Ni-LCCM	0.50	2Ni-LCCM	11.53	2.58
075Ni-LCCM	0.75	3Ni-LCCM	9.86	4.39
100Ni-LCCM	1.00	4Ni-LCCM	10.34	4.76
125Ni-LCCM	1.25	5Ni-LCCM	10.13	4.25
150Ni-LCCM	1.50	6Ni-LCCM	11.05	3.45
175Ni-LCCM	1.75	7Ni-LCCM	10.61	4.35
200Ni-LCCM	2.00	8Ni-LCCM	10.27	4.05

The yNi-LCCM models are representative computational models used to describe different relative Ni-loading levels and local Ni configurations, rather than the exact bulk stoichiometry of the experimental samples. For Ni-free LCCM, Ni-normalized carbon productivity is not applicable; LCCM is included as a reference because negligible carbon formation was observed. The rate-limiting barrier refers to the highest activation barrier among the elementary C-H bond cleavage steps considered in the DFT calculations. DFT: Density functional theory; LCCM: $(La_{0.75}Ca_{0.25})(Cr_{0.5}Mn_{0.5})O_{3-\delta}$.

The origin of this non-monotonic Ni utilization is further examined by density functional theory calculations in the following section, where the experimental Ni-normalized carbon productivities are correlated with representative DFT-derived rate-limiting barriers in Table 2. A comparison of carbon productivity and reaction conditions for representative Ni-based methane decomposition catalysts is provided in Supplementary Table 3. Because reported carbon yields are normalized using different bases across studies, this comparison is intended only as a contextual benchmark rather than a direct ranking.

DFT analysis of Ni-configuration-dependent methane decomposition

DFT calculations were performed to examine elementary C-H bond-cleavage steps, adsorption behavior, and activation barriers (E_a) associated with methane decomposition. To rationalize the experimentally observed non-monotonic Ni-normalized carbon productivity, calculations were carried out on LCCM, Ni(111), and representative yNi-LCCM surface models with different relative Ni-loading levels and local Ni configurations. As shown in Figure 7A and B, Ni(111) and the LCCM(0-10) surface were first constructed as reference models, representing metallic Ni and the parent LCCM surface, respectively. These two reference structures provide the baseline for evaluating the effects of progressively introduced Ni species and their local configurations in the yNi-LCCM models. The LCCM surface model was constructed based on XRD refinement [Supplementary Figure 10], and the corresponding surface configuration is shown in Supplementary Figure 11. Ni atoms were introduced into the LCCM surface model to represent increasing relative Ni-loading levels, followed by structural optimization [Figure 7C-J]. As defined in Table 1, the yNi-LCCM models serve as representative computational analogs of the experimental xNi-LCCM series, rather than exact bulk stoichiometric replicas. The correlation between the experimental Ni-normalized carbon productivity and the DFT-derived rate-limiting barriers is summarized in Table 2. Ni(111) was included as a reference surface because it is a stable and commonly used model for metallic Ni in methane decomposition studies[49].

The stepwise C-H bond cleavage pathway of methane was modeled through four elementary dehydrogenation steps from surface-bound CH_4 to surface carbon species. Transition-state calculations were used to determine the activation energy for each elementary C-H bond cleavage step. The rate-limiting step was defined as the elementary step with the highest activation barrier for each surface. The elementary C-H bond cleavage steps are listed in Supplementary Table 4, and the calculated activation energies are summarized in Supplementary Table 5. The rate-limiting barriers extracted from Supplementary Table 5 are

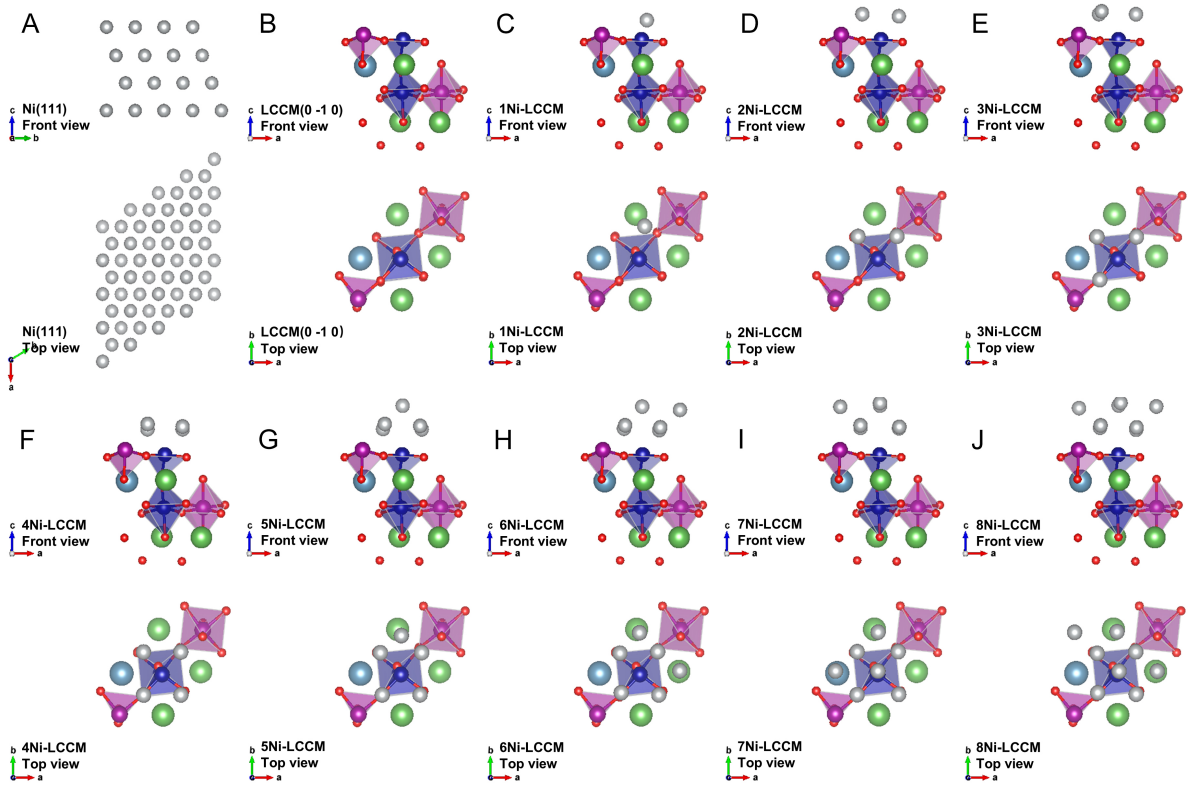

Figure 7. Optimized surface configurations of (A) Ni(111), (B) LCCM, and (C-J) yNi-LCCM surfaces (y = 1 - 8). Each panel shows the front and top views of the optimized model. Colors denote different elements: La (green), Ca (light blue), Cr (dark blue), Mn (purple), Ni (white/grey), and O (red). LCCM: $(La_{0.75}Ca_{0.25})(Cr_{0.5}Mn_{0.5})O_{3-\delta}$.

compared with the experimental Ni-normalized carbon productivities in Table 2. A schematic illustration of the methane decomposition pathway and surface intermediates is shown in Supplementary Figure 12. Hydrogen recombination and desorption were treated in a simplified manner and were not used to define the rate-limiting C-H activation barriers.

Reaction energy profiles are shown in Figure 8, and the corresponding rate-limiting activation energies are summarized in Table 2 and Supplementary Table 5. Comparison across different Ni loadings reveals a non-monotonic variation in the rate-limiting activation energy. Among the yNi-LCCM models, 2Ni-LCCM and 6Ni-LCCM exhibit lower rate-limiting barriers than neighboring compositions, indicating more favorable C-H bond cleavage kinetics. These two models serve as representative computational analogs of the experimental 050Ni-LCCM and 150Ni-LCCM compositions, respectively. As summarized in Table 2, the lower calculated barriers for 2Ni-LCCM and 6Ni-LCCM are consistent with the experimentally observed local maxima in Ni-normalized carbon productivity. This comparison suggests that the non-monotonic carbon productivity is closely related to the local reaction energetics of composition-tuned Ni sites.

Further insight is obtained from the optimized surface configurations [Figure 7]. At lower Ni loadings, Ni atoms are primarily located in the surface layer of the LCCM model, whereas additional Ni atoms occupy second-layer configurations at higher loadings. In the present models, up to four Ni atoms can be accommodated near the surface before excess Ni preferentially occupies subsurface or second-layer positions. This transition alters the local coordination environment and Ni-Ni ensemble structure of the active sites.

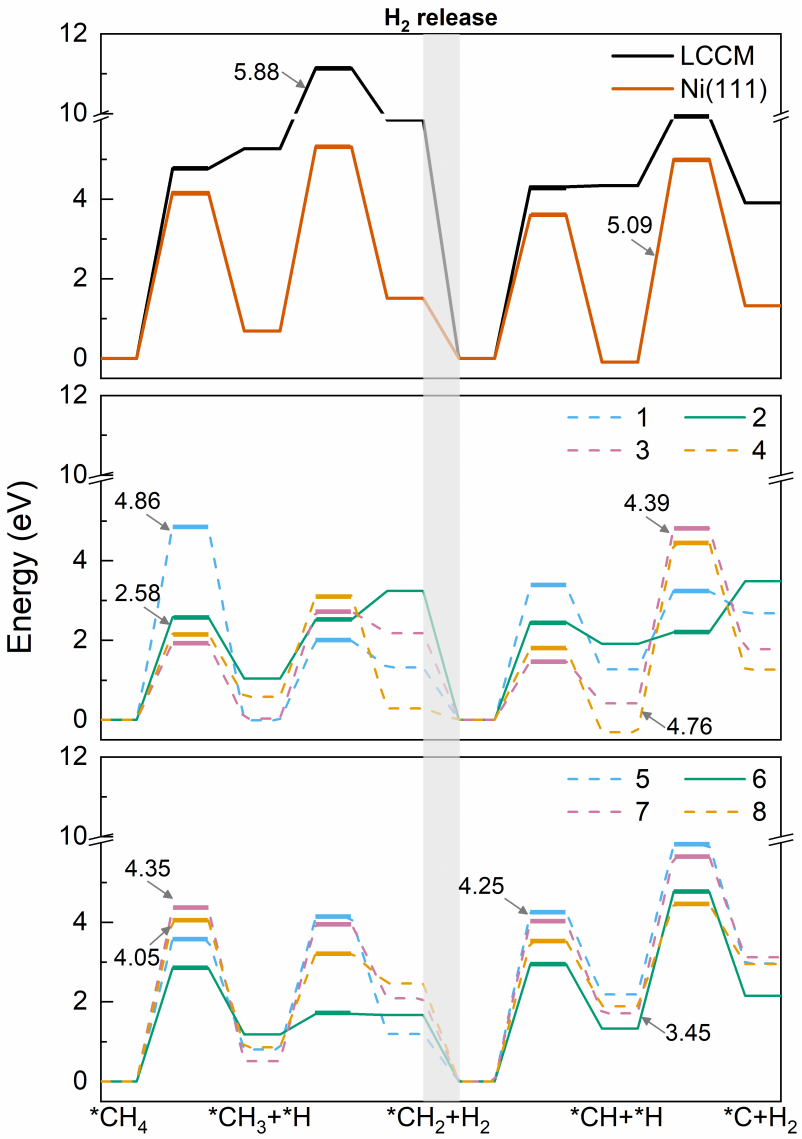

Figure 8. Reaction energy profiles for methane decomposition on LCCM, Ni(111), and yNi-LCCM surfaces (y = 1-8). The grey region highlights the simplified hydrogen-release step. LCCM: $(La_{0.75}Ca_{0.25})(Cr_{0.5}Mn_{0.5})O_{3-\delta}$.

The calculated low-barrier compositions, particularly 050Ni-LCCM and 150Ni-LCCM, correspond to favorable surface Ni configurations before extensive second-layer Ni occupation. With further increases in Ni loading, additional Ni atoms increasingly contribute to Ni-Ni ensemble or bulk-like behavior rather than improving the intrinsic activity of each Ni site. This provides a possible explanation for why increasing Ni content enhances overall methane conversion and catalyst-mass-normalized carbon yield but does not lead to a proportional increase in Ni-normalized carbon productivity.

Overall, the DFT results help rationalize the experimental observation that Ni utilization in xNi-LCCM is not controlled by total Ni content alone, but is strongly influenced by local Ni configuration, Ni reducibility, and site accessibility. This interpretation is consistent with the structural and surface analyses discussed above: XRD confirms the stability of the LCCM framework after reduction, XPS shows the coexistence of Ni^0 and Ni^{2+} species, STEM-EDS reveals reduction-induced Ni redistribution, and HRTEM indicates interfacial anchoring of Ni-containing domains on the LCCM matrix. These findings suggest that composition-tuned, exsolution-related Ni configurations play an important role in determining methane decomposition activity

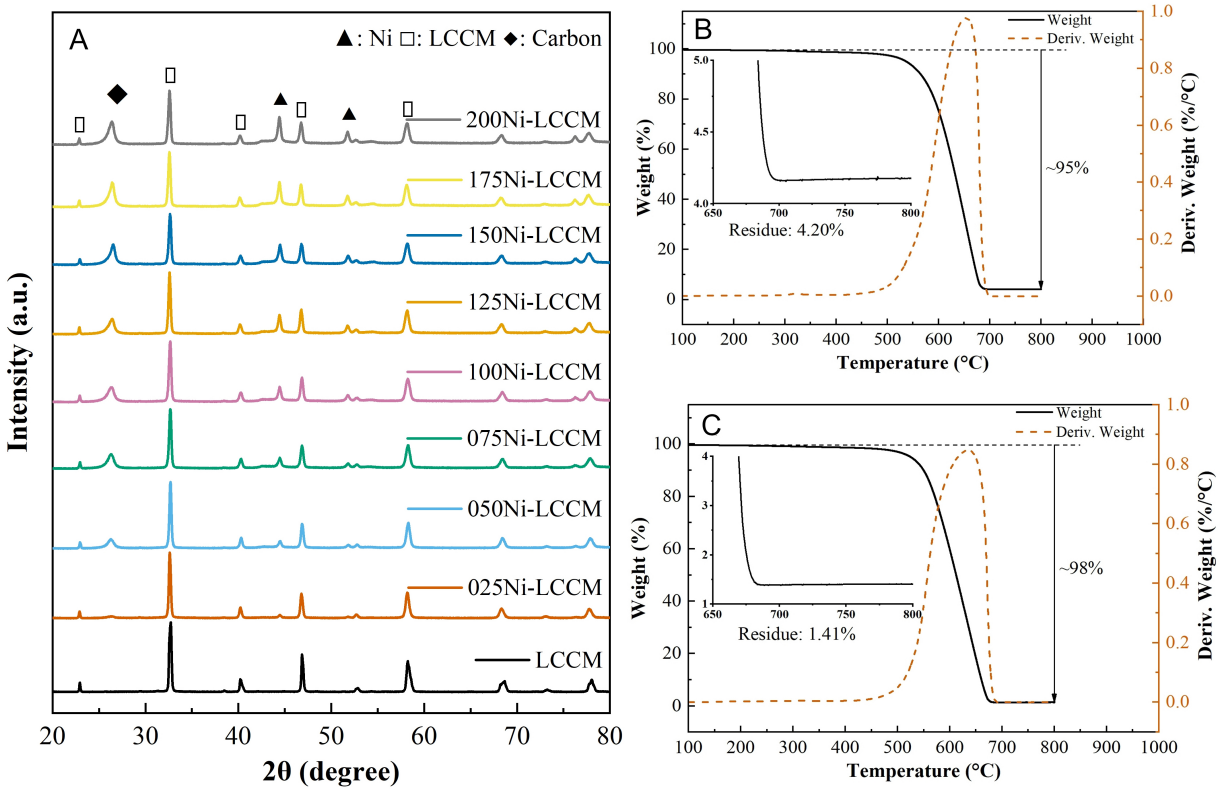

Figure 9. Carbon phase formation and residual inorganic content of xNi-LCCM-derived carbon products. (A) XRD patterns of spent LCCM and xNi-LCCM catalysts after methane decomposition at 750 °C for 8 h. Diffraction peaks corresponding to LCCM, metallic Ni, and graphitic carbon are marked; (B and C) TGA and derivative weight curves of acid-treated carbon products obtained from (B) 050Ni-LCCM and (C) 150Ni-LCCM after treatment with 5 M HNO_3. The residual masses after carbon oxidation were used to estimate the remaining inorganic contents. XRD: X-ray diffraction; TGA: thermogravimetric analysis; LCCM: $(La_{0.75}Ca_{0.25})(Cr_{0.5}Mn_{0.5})O_{3-\delta}$.

and intrinsic carbon productivity.

Carbon characterization

Figure 9A presents the XRD patterns of the spent LCCM and xNi-LCCM catalysts after methane decomposition at 750 °C for 8 h. For the Ni-containing samples, diffraction peaks corresponding to metallic Ni are observed, which can be attributed to the in situ reduction of Ni species under the methane reaction environment. Additional diffraction features at $2\theta \approx 26.3$-$26.5°$ are assigned to graphitic carbon formed during CDM. In contrast, no diffraction peaks associated with either metallic Ni or graphitic carbon are observed for the Ni-free LCCM sample, indicating that the LCCM support remains structurally stable and shows negligible activity toward methane decomposition under the investigated conditions.

The carbon-catalyst mixture collected after methane decomposition was subsequently treated with 5 M HNO_3 to separate the carbon product from the catalyst. The purified carbon was analyzed by TGA to estimate the remaining inorganic content. As shown in Figure 9B and C, the mass loss below 200 °C is attributed to moisture removal, while the major mass loss between 200 and 800 °C corresponds to carbon oxidation. The residual mass at higher temperatures was assigned to inorganic residue. After acid treatment, the residual masses were 4.20 % and 1.41 % for the carbon products from 050Ni-LCCM and 150Ni-LCCM, respectively, corresponding to TGA-based carbon contents of approximately 95.8% and 98.6%. This indicates effective removal of most inorganic species from the carbon product. Notably, this purification was achieved using relatively mild nitric acid treatment, compared with the stronger acid conditions typically required for chemically stable oxide supports such as TiO_2 and SiO_2[50].

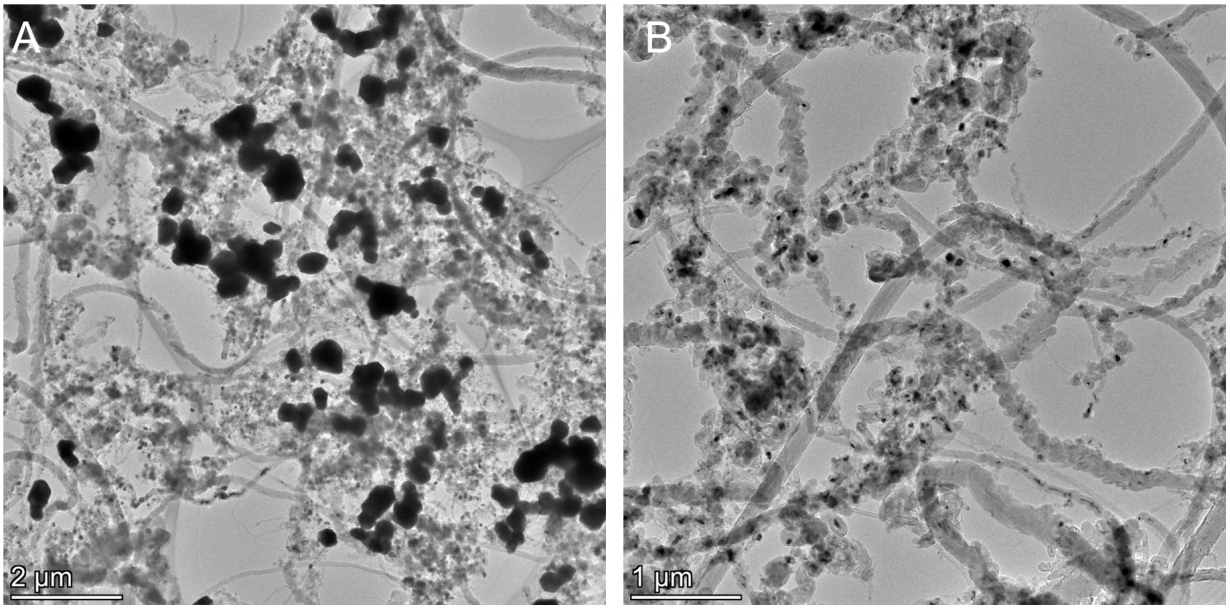

Figure 10. Representative TEM images of carbon-catalyst mixture after 8 h CDM reaction: (A) before acid treatment and (B) after acid treatment with 5 M HNO_3. Dark contrast regions associated with catalyst particles are significantly reduced after acid treatment, while the overall carbon morphology is preserved. TEM: Transmission electron microscopy; CDM: catalytic decomposition of methane.

Figure 10 shows representative TEM images of the carbon-catalyst mixture before and after acid treatment. Before acid washing, dark contrast regions are observed and are attributed to catalyst particles. After treatment with 5 M HNO_3, these regions are largely removed, indicating effective separation of the catalyst from the carbon product. The overall carbon morphology is largely retained after acid treatment, suggesting that the acid washing step mainly removes the inorganic catalyst component without causing obvious structural damage to the carbon framework. TEM analysis also shows that the carbon product contains mixed nanostructures, including carbon nanotubes, carbon nanofibers, and carbon nano-onions.

Raman spectroscopy was performed to evaluate the structural ordering of the carbon products before and after acid treatment. The spectra were baseline-corrected and deconvoluted using Lorentzian functions to analyze the D, G, and 2D bands. The D band at ~1,350 cm^{-1} is associated with defect-induced vibrational modes, while the G band at ~1,580 cm^{-1} corresponds to the in-plane stretching vibration of sp^2-hybridized carbon[38]. The D/G intensity ratio (I_D/I_G) was used to assess the structural ordering of the carbon products, with lower values indicating fewer defects and higher graphitic order.

The mean I_D/I_G values of the carbon products ranged from approximately 0.74 to 0.90 before acid washing and from approximately 0.62 to 0.75 after acid treatment [Figure 11]. The decrease in I_D/I_G after purification suggests improved apparent graphitic ordering, which is mainly attributed to the removal of disordered carbon species and residual catalyst-related impurities rather than direct structural transformation of the carbon framework. Together with the relatively high oxidation temperature observed in TGA and the tubular carbon morphologies observed by TEM, the well-defined D, G, and 2D bands indicate that the carbon products are predominantly nanocrystalline graphitic carbon rather than amorphous carbon.

CONCLUSIONS

Ni-LCCM catalysts were developed and evaluated for catalytic methane decomposition using a nitrate-based gel-casting route. Under the optimized reaction condition of 750 °C, 050Ni-LCCM achieved a high Ni-normalized carbon productivity of 11.53 $g_C \cdot g_{Ni}^{-1}$, indicating efficient utilization of active Ni species.

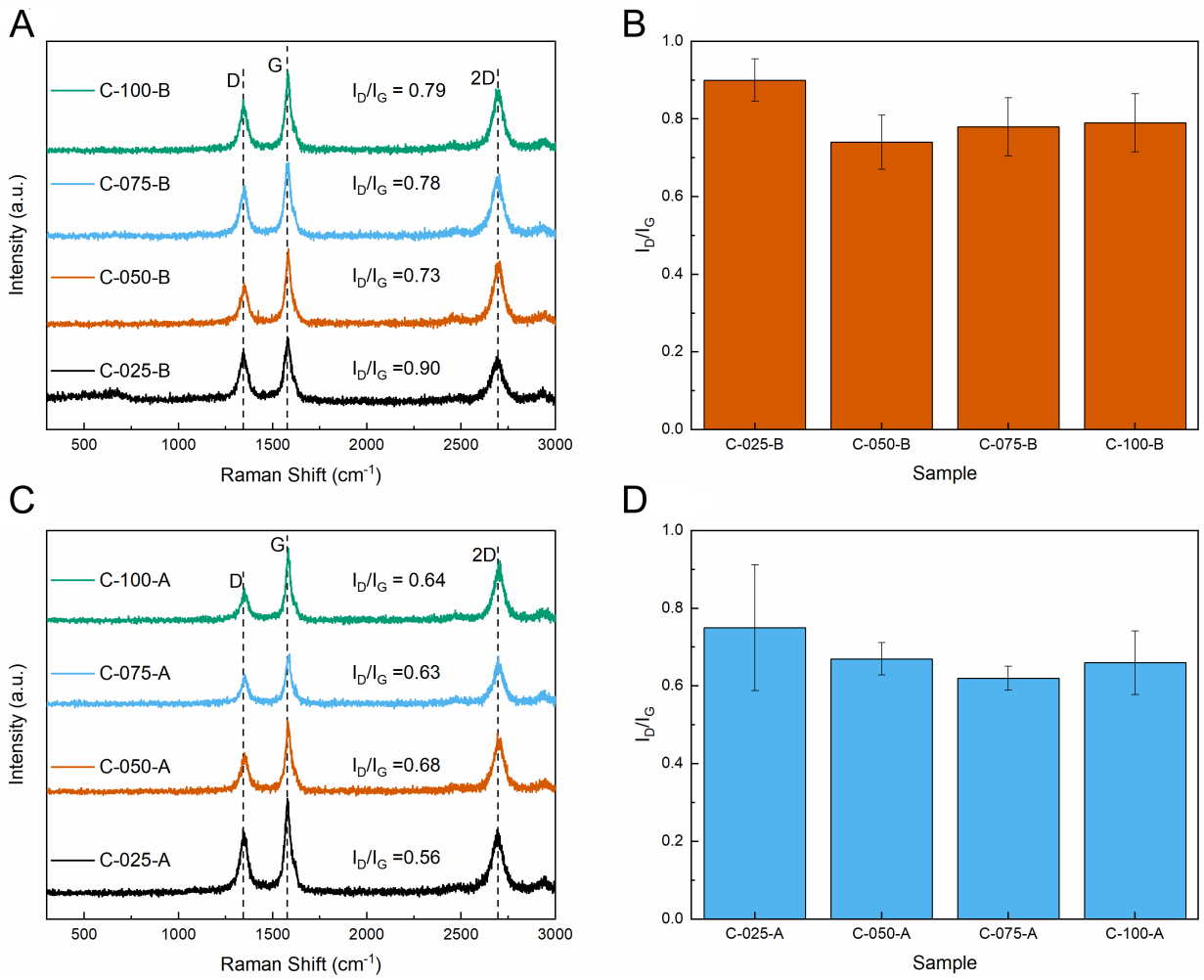

Figure 11. Raman spectra of carbon-catalyst mixtures after 8 h CDM reaction and acid-washed carbon treated with 5 M HNO_3: (A and C) Raman spectra before and after acid treatment, respectively; (B and D) corresponding I_D/I_G ratios. The D, G, and 2D bands are indicated. The ID/IG values annotated in (A and C) correspond to the representative spectra shown, whereas the bars in (B and D) represent the mean ID/IG values obtained from three Raman spectra collected from different regions of each sample; error bars indicate the corresponding standard deviations. CDM: Catalytic decomposition of methane.

A non-monotonic dependence of intrinsic carbon productivity on Ni loading was observed. The highest Ni-normalized carbon productivities occurred for 050Ni-LCCM and 150Ni-LCCM, while neighboring compositions showed lower values. DFT calculations showed lower relative rate-limiting activation barriers for the corresponding 2Ni-LCCM and 6Ni-LCCM models. Combined with the catalytic and structural characterization results, this suggests that methane decomposition activity is strongly influenced by local Ni configuration, Ni reducibility, and site accessibility rather than by total Ni content alone.

Carbon characterization confirmed the formation of predominantly nanocrystalline graphitic carbon. TEM analysis showed mixed carbon nanostructures, while Raman spectroscopy showed a decrease in the mean I_D/I_G values from approximately 0.74-0.90 to 0.62-0.75 after acid treatment. Together with TGA oxidation at ~600-700 °C, these results indicate that the carbon products are mainly graphitic rather than amorphous.

Post-reaction purification using 5 M HNO_3 effectively separated the carbon product from the catalyst. The residual inorganic contents were reduced to 4.20% and 1.41% for carbon products from 050Ni-LCCM and 150Ni-LCCM, respectively, corresponding to TGA-based carbon contents of approximately 95.8% and 98.6%. The overall carbon morphology was largely retained after acid treatment.

Overall, this work demonstrates that Ni-LCCM is an effective catalyst system for CDM, where optimized Ni configurations enhance intrinsic activity while enabling recovery of high-carbon-content solid products after mild acid treatment. Further optimization of reaction conditions may improve control over carbon morphology and product selectivity.

DECLARATIONS

Author's contributions

Conceptualization, methodology, investigation, data curation, formal analysis, visualization, writing - original draft: Chua, S. R.

Methodology, software, investigation, data curation, formal analysis, visualization, writing - review and editing: Wang, R.

Investigation, data curation: He, H.; Cao, X.

Writing - review and editing: Deng, Z.; Xiao, G.; Wang, J.; Zhang, L. (Lili Zhang); Poh, C. K.

Conceptualization, methodology, supervision, writing - review and editing: Zhang, L. (Lan Zhang)

Supervision, writing - review and editing: Ni, M.; Chan, S. H.

Availability of data and materials

The original contributions presented in this study are included in the article/Supplementary Materials. Further inquiries can be directed to the corresponding author(s).

AI and AI-assisted tools statement

During the preparation of this manuscript, multiple versions of ChatGPT (OpenAI) were used solely for language editing over the course of manuscript preparation. The tool did not influence the study design, data collection, analysis, interpretation, or the scientific content of the work. All authors take full responsibility for the accuracy, integrity, and final content of the manuscript.

Financial support and sponsorship

The research is supported by grants from the Research Grants Council (Project numbers: SRFS2324-5S02 and 15304825) and the University Grants Committee, HK SAR. The authors gratefully acknowledge financial support from A*STAR's Central Research Fund. This work was supported by the Fundamental Research Program of Industrial Foundation (SINAP-CYJJ-202502).

Conflicts of interest

All authors declared that there are no conflicts of interest.

Ethical approval and consent to participate

Not applicable.

Consent for publication

Not applicable.

Supplementary Materials

Supplementary Materials

REFERENCES

1. Ishaq, H.; Dincer, I.; Crawford, C. A review on hydrogen production and utilization: Challenges and opportunities. *Int. J. Hydrogen. Energy.* **2022**, *47*, 26238-64. DOI
2. Hermesmann, M.; Müller, T. Green, turquoise, blue, or grey? Environmentally friendly hydrogen production in transforming energy systems. *Prog. Energy. Combust. Sci.* **2022**, *90*, 100996. DOI

3. Tong, S.; Miao, B.; Zhang, W.; Zhang, L.; Chan, S. H. Optimization of methane catalytic decomposition in a fluidized bed reactor: a computational approach. *Energy. Convers. Manag.* **2023**, *297*, 117719. DOI
4. Zainal, B. S.; Ker, P. J.; Mohamed, H.; et al. Recent advancement and assessment of green hydrogen production technologies. *Renew. Sustain. Energy. Rev.* **2024**, *189*, 113941. DOI
5. Shokrollahi, M.; Teymouri, N.; Ashrafi, O.; Navarri, P.; Khojasteh-salkuyeh, Y. Methane pyrolysis as a potential game changer for hydrogen economy: techno-economic assessment and GHG emissions. *Int. J. Hydrogen. Energy.* **2024**, *66*, 337-53. DOI
6. Qian, J. X.; Chen, T. W.; Enakonda, L. R.; Liu, D. B.; Basset, J.; Zhou, L. Methane decomposition to pure hydrogen and carbon nano materials: State-of-the-art and future perspectives. *Int. J. Hydrogen. Energy.* **2020**, *45*, 15721-43. DOI
7. Pinilla, J.; Utrilla, R.; Lázaro, M.; Moliner, R.; Suelves, I.; García, A. Ni- and Fe-based catalysts for hydrogen and carbon nanofilament production by catalytic decomposition of methane in a rotary bed reactor. *Fuel. Process. Technol.* **2011**, *92*, 1480-8. DOI
8. Lua, A. C.; Wang, H. Y. Decomposition of methane over unsupported porous nickel and alloy catalyst. *Appl. Catal. B. Environ.* **2013**, *132-133*, 469-78. DOI
9. Moghaddam, A. L.; Hejazi, S.; Fattahi, M.; et al. Methane pyrolysis for hydrogen production: navigating the path to a net zero future. *Energy. Environ. Sci.* **2025**, *18*, 2747-90. DOI
10. Sun, E.; Zhai, S.; Kim, D.; et al. A semi-continuous process for co-production of CO_2-free hydrogen and carbon nanotubes via methane pyrolysis. *Cell. Rep. Phys. Sci.* **2023**, *4*, 101338. DOI
11. Bayat, N.; Meshkani, F.; Rezaei, M. Thermocatalytic decomposition of methane to CO_x-free hydrogen and carbon over Ni-Fe-Cu/Al_2O_3 catalysts. *Int. J. Hydrogen. Energy.* **2016**, *41*, 13039-49. DOI
12. Ahmad, A.; Hamdani, I. R.; Srinivasakannan, C.; Al Shoaibi, A.; Hossain, M. M. Catalytic cracking of methane to hydrogen and carbon: scale-up perspective. *Int. J. Hydrogen. Energy.* **2024**, *54*, 1212-30. DOI
13. Ahmed, H.; Alotibi, M. F.; Fakeeha, A. H.; et al. Hydrogen production via methane decomposition over alumina doped with titanium oxide-supported iron catalyst for various calcination temperatures. *ChemistryOpen* **2024**, *13*, e202300173. DOI
14. Feng, F.; Song, G.; Xiao, J.; Shen, L.; Pisupati, S. V. Carbon deposition on Ni-based catalyst with TiO_2 as additive during the syngas methanation process in a fluidized bed reactor. *Fuel* **2019**, *235*, 85-91. DOI
15. Busillo, E.; Damizia, M.; De Filippis, P.; de Caprariis, B. Methane pyrolysis in molten media: the interplay of physical properties and catalytic activity on carbon and hydrogen production. *J. Anal. Appl. Pyrolysis.* **2024**, *183*, 106752. DOI
16. Sanyal, A.; Malalasekera, W.; Bandulasena, H.; Wijayantha, K. Review of the production of turquoise hydrogen from methane catalytic decomposition: optimising reactors for sustainable hydrogen production. *Int. J. Hydrogen. Energy.* **2024**, *72*, 694-715. DOI
17. Polo-garzon, F.; Fung, V.; Liu, X.; et al. Understanding the impact of surface reconstruction of perovskite catalysts on CH_4 activation and combustion. *ACS. Catal.* **2018**, *8*, 10306-15. DOI
18. Neagu, D.; Tsekouras, G.; Miller, D. N.; Ménard, H.; Irvine, J. T. In situ growth of nanoparticles through control of non-stoichiometry. *Nat. Chem.* **2013**, *5*, 916-23. DOI PubMed
19. Jardiel, T.; Caldes, M.; Moser, F.; Hamon, J.; Gauthier, G.; Joubert, O. New SOFC electrode materials: the Ni-substituted LSCM-based compounds $(La_{0.75}Sr_{0.25})(Cr_{0.5}Mn_{0.5-x}Ni_x)O_{3-\delta}$ and $(La_{0.75}Sr_{0.25})(Cr_{0.5-x}Ni_xMn_{0.5})O_{3-\delta}$. *Solid. State. Ionics.* **2010**, *181*, 894-901. DOI
20. Sun, H.; He, X.; Huang, X.; Gan, L. Modification of LSCM structure by anchoring alloy nanoparticles for efficient CO_2 electrolysis. *Energy. Fuels.* **2024**, *38*, 3436-44. DOI
21. Neagu, D.; Oh, T. S.; Miller, D. N.; et al. Nano-socketed nickel particles with enhanced coking resistance grown in situ by redox exsolution. *Nat. Commun.* **2015**, *6*, 8120. DOI PubMed PMC
22. Yu, J.; Liu, X.; Zhong, M.; et al. Suppression of Sr segregation in $La_{0.6}Sr_{0.4}Co_{0.2}Fe_{0.8}O_{3-\delta}$ oxygen electrode via Ca doping for enhanced performance stability of reversible solid oxide cell. *ACS. Appl. Mater. Interfaces.* **2026**, *18*, 11409-20. DOI
23. Koo, B.; Kim, K.; Kim, J. K.; Kwon, H.; Han, J. W.; Jung, W. Sr segregation in perovskite oxides: why it happens and how it exists. *Joule* **2018**, *2*, 1476-99. DOI
24. Zhang, L.; Zhang, W.; Poh, C. K.; et al. Catalytic decomposition of methane: Ni-promoted perovskite oxide catalysts for turquoise hydrogen and carbon nanomaterials Co-production. *Energy. Mater.* **2025**, *5*, 500023. DOI
25. Perdew, J. P.; Burke, K.; Ernzerhof, M. Generalized gradient approximation made simple. *Phys. Rev. Lett.* **1996**, *77*, 3865-8. DOI PubMed
26. Monkhorst, H. J.; Pack, J. D. Special points for Brillouin-zone integrations. *Phys. Rev. B.* **1976**, *13*, 5188-92. DOI
27. Jónsson, H.; Mills, G.; Jacobsen, K. W. Nudged elastic band method for finding minimum energy paths of transitions. In *Classical and Quantum Dynamics in Condensed Phase Simulations*, LERICI, Villa Marigola, July 7-18, 1997; Berne B. J.; Ciccotti, G.; Coker, D. F.; Eds.; World Scientific, 1997; pp 385-404. DOI
28. Henkelman, G.; Uberuaga, B. P.; Jónsson, H. A climbing image nudged elastic band method for finding saddle points and minimum energy paths. *J. Chem. Phys.* **2000**, *113*, 9901-4. DOI

29. Vera, E.; Trillaud, V.; Metaouaa, J.; et al. Comparative study of exsolved and impregnated Ni nanoparticles supported on nanoporous perovskites for low-temperature CO oxidation. *ACS. Appl. Mater. Interfaces.* **2024**, *16*, 7219-31. DOI
30. Flores-lasluisa, J.; Huerta, F.; Cazorla-amorós, D.; Morallón, E. $LaNi_{1-x}Co_xO_3$ perovskites for application in electrochemical reactions involving molecular oxygen. *Energy* **2023**, *273*, 127256. DOI
31. Khan, U. M.; Sarmad, Q.; Anwar, M.; et al. Synthesis of cobalt loaded double perovskite $Sr_2TiFeO_{6-\delta}$ (STF) as a stable catalyst for enhanced hydrogen production via methane decomposition. *Int. J. Energy. Res.* **2021**, *45*, 20073-88. DOI
32. Rudolph, B.; Tsiotsias, A. I.; Ehrhardt, B.; et al. Nanoparticle exsolution from nanoporous perovskites for highly active and stable catalysts. *Adv. Sci.* **2023**, *10*, e2205890. DOI PubMed PMC
33. Piazzolla, F.; Moraes, T. S.; Figueiredo, S. S.; et al. Exsolution of Ni nanoparticles from $La_{0.4}Sr_{0.4}Ti_{0.8}Ni_{0.2}O_{3-\delta}$ perovskite for ethanol steam reforming. *Catal. Today.* **2025**, *444*, 115011. DOI
34. Qiao, L.; Bi, X. Direct observation of Ni^{3+} and Ni^{2+} in correlated $LaNiO_{3-\delta}$ films. *EPL* **2011**, *93*, 57002. DOI
35. Whitten, A.; Guo, D.; Tezel, E.; Denecke, R.; Nikolla, E.; McEwen, J. S. Deconvoluting XPS spectra of La-containing perovskites from first-principles. *JACS. Au.* **2024**, *4*, 3104-17. DOI PubMed PMC
36. Barreau, M.; Salusso, D.; Zhang, J.; et al. Uncovering the critical function of lanthanum in CH_4 production from CO_2 using exsolved $LaNiO_3$ perovskite catalysts. *J. Mater. Chem. A.* **2024**, *12*, 7605-21. DOI
37. Vargas, N. F. C.; Alkathy, M. S.; Eiras, J. A.; Mastelaro, V. R.; Lente, M. H. Sintering-driven effects on the band gap of $(Pb,La)(Ti,Ni)O_3$ photovoltaic ceramics. *J. Am. Ceram. Soc.* **2021**, *104*, 2600-9. DOI
38. Sun, Z.; Gong, Y.; Cheng, D.; Sun, Z. Reinforcing hydrogen and carbon nanotube co-production via Cr-O-Ni catalyzed methane decomposition. *J. Mater. Chem. A.* **2024**, *12*, 4893-902. DOI
39. Sunding, M.; Hadidi, K.; Diplas, S.; Løvvik, O.; Norby, T.; Gunnæs, A. XPS characterisation of in situ treated lanthanum oxide and hydroxide using tailored charge referencing and peak fitting procedures. *J. Electron. Spectrosc. Relat. Phenom.* **2011**, *184*, 399-409. DOI
40. Soltani, N.; Arcos, L. H.; Bahrami, A.; Carvayar, J. C. Structural changes in $NiO\text{-}Ce_{0.8}Sm_{0.2}O_{2-x}$ anode under reducing atmosphere. *Mater. Charact.* **2019**, *150*, 8-12. DOI
41. Ning, X.; Wang, Z.; Zhang, Z. Fermi level shifting, charge transfer and induced magnetic coupling at $La_{0.7}Ca_{0.3}MnO_3/LaNiO_3$ interface. *Sci. Rep.* **2015**, *5*, 8460. DOI PubMed PMC
42. Hillebrecht, F. U.; Fuggle, J. C.; Bennett, P. A.; Zołnierek, Z.; Freiburg, C. Electronic structure of Ni and Pd alloys. II. X-ray photoelectron core-level spectra. *Phys. Rev. B.* **1983**, *27*, 2179-93. DOI
43. Cao, P.; Tang, P.; Bekheet, M. F.; et al. Atomic-scale insights into nickel exsolution on $LaNiO_3$ catalysts via in situ electron microscopy. *J. Phys. Chem. C.* **2022**, *126*, 786-96. DOI
44. Wei, Y.; Zheng, Y.; Hu, Y.; et al. Controlling the cation exsolution of perovskite to customize heterostructure active site for oxygen evolution reaction. *ACS. Appl. Mater. Interfaces.* **2022**, *14*, 25638-47. DOI
45. Anjaneyulu, C.; Naresh, G.; Kumar, V. V.; Tardio, J.; Rao, T. V.; Venugopal, A. Influence of rare earth (La, Pr, Nd, Gd, and Sm) metals on the methane decomposition activity of Ni-Al catalysts. *ACS. Sustainable. Chem. Eng.* **2015**, *3*, 1298-305. DOI
46. Garbarino, G.; Kowalik, P.; Riani, P.; et al. Improvement of Ni/Al_2O_3 catalysts for low-temperature CO_2 methanation by vanadium and calcium oxide addition. *Ind. Eng. Chem. Res.* **2021**, *60*, 6554-64. DOI
47. Zhang, T.; Liu, Z.; Zhu, Y.; et al. Dry reforming of methane on Ni-Fe-MgO catalysts: influence of Fe on carbon-resistant property and kinetics. *Appl. Catal. B. Environ.* **2020**, *264*, 118497. DOI
48. Osti, A.; Costa, S.; Rizzato, L.; Senoner, B.; Glisenti, A. Photothermal activation of methane dry reforming on perovskite-supported Ni-catalysts: impact of support composition and Ni loading method. *Catal. Today.* **2025**, *449*, 115200. DOI
49. Helveg, S.; López-Cartes, C.; Sehested, J.; et al. Atomic-scale imaging of carbon nanofibre growth. *Nature* **2004**, *427*, 426-9. DOI
50. Bossert, D.; Urban, D. A.; Maceroni, M.; et al. A hydrofluoric acid-free method to dissolve and quantify silica nanoparticles in aqueous and solid matrices. *Sci. Rep.* **2019**, *9*, 7938. DOI PubMed PMC